RICE UNIVERSITY

GDOT: Gated Diffuse Optical Tomography

By

Yongyi Zhao

A THESIS SUBMITTED
IN PARTIAL FULFILLMENT OF THE
REQUIREMENTS FOR THE DEGREE

Master of Science

APPROVED, THESIS COMMITTEE

Ashok Veeraraghavan (Apr 28, 2021 11:28 CDT)

Ashok Veeraraghavan

Professor of Electrical and Computer
Engineering and Computer Science

Caleb Kemere

Associate Professor of Electrical and
Computer Engineering and Bioengineering

Jacob Robinson (Mar 9, 2021 11:40 CST)

Jacob Robinson

Associate Professor of Electrical and
Computer Engineering and Bioengineering

Ashutosh Sabharwal (Mar 9, 2021 09:34 PST)

Ashutosh Sabharwal

Earnest Dell Butcher Professor of Electrical
and Computer Engineering

HOUSTON, TEXAS

March 2021

ABSTRACT

GDOT: Gated Diffuse Optical Tomography

by

Yongyi Zhao

Time-of-flight diffuse optical tomography (ToF-DOT) is a promising technology for non-invasive functional neuroimaging. Such an imaging device could lead to wearable brain-computer interfaces (BCIs) for prosthetics and faster communication. Unfortunately, ToF-DOT suffers from low spatial resolution and poor temporal resolution. The low spatial resolution is caused by the scattering of light in biological tissue and complex electronics, which limit the detector size. The poor temporal resolution is due to the large volume of measurements that must be transferred and processed. To address these challenges, we propose Gated Diffuse Optical Tomography (GDOT). GDOT uses time-gating to mitigate the effects of optical scattering while reducing the hardware and computational complexity associated with collecting full light transport transients. To demonstrate the capabilities of our proposed system, we conducted a simulated performance analysis and image reconstruction on experimental data collected from our prototype system. We showed over two orders of magnitude reduction in the algorithm runtime and enhanced image reconstruction quality using our GDOT technique.

Acknowledgments

Contents

Illustrations

Chapter 1

Introduction

Over the past few years, there has been increasing interest in brain-computer interface (BCIs), a technology that can extract signals from neural activity and convert these signals into the input for an external device [4]. Such a technology could lead to increased control and flexibility for prosthetic devices [4], novel approaches to providing input to a computer [4, 5], and a faster means of inter-person communication, which would not require any verbal or physical signaling [6]. The first step to constructing a BCI would be to extract the neural signals, i.e., to perform functional neuroimaging. To be of practical use, such a device would need to satisfy certain criteria. Namely, it would need to be safe, portable, and achieve high temporal and spatial resolution (figure 1.1). While several technologies have been developed for functional neuroimaging, no existing device satisfies all four requirements of an ideal BCI. Here we will briefly review a subset of these existing technologies, including functional magnetic resonance imaging (fMRI), electroencephalogram (EEG), and optical imaging, before delving into how we can advance the state-of-the-art with our proposed technology.

fMRI: In functional magnetic resonance imaging, neural activity is correlated with a surrogate signal, known as the blood-oxygenation-level-dependent (BOLD) signal [7]. The BOLD signal produces a change in the magnetic field, which can be detected by the MRI [7]. This technology achieves a relatively high spatial resolution of approximately 1 mm [7]. Unfortunately, the primary limitation of fMRI is its immobility since the patient must be placed in a bulky apparatus and cannot move
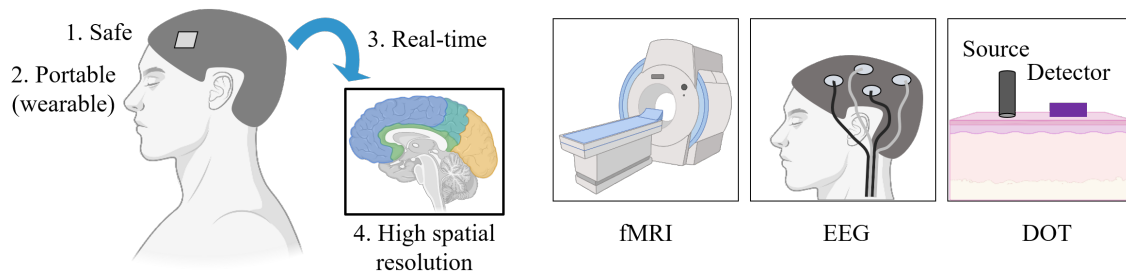
Figure 1.1 : **Objectives:** The diagram on the left shows an overview of our ultimate goal, which is to construct a wearable functional neuroimaging device that is safe, portable, fast (performs in real-time), and accurate (achieves high spatial resolution). On the right, we include current methods for performing non-invasive, functional neuroimaging.

during the procedure. This is an enormous limitation, as many applications and potential neurological studies require the patient to be mobile.

EEG: EEG measures neural activity by recording the voltage-based signals directly through the skull and scalp. EEG can be built into a compact, wearable form factor. Unfortunately, this voltage-based signal is heavily attenuated and blurred as it passes through the human skull, resulting in low spatial resolution on the order of centimeters [4]. This makes EEG also impractical in the application of BCIs.

1.1   Optical Imaging

Optical imaging is safe, can be built into a compact form factor, and is relatively inexpensive [8, 9]. However, one of the greatest challenges for optical imaging is the optical scattering of light, which results in reduced contrast and lower spatial resolution [9]. Thus, to construct the desired high-spatial-resolution, fast, wearable imaging technology using optical imaging techniques, one must first mitigate the effects of optical scattering.

1.1.1 Ballistic Imaging

One approach to reducing the effects of scattering is ballistic imaging. Such imaging techniques focus on the unscattered photons, which are referred to as ballistic photons. A variety of techniques are used to filter out the diffuse photons and extract only the ballistic photons. One example is confocal microscopy [10, 2]. The core idea of confocal microscopy is to use spatial filtering. This can be achieved by incorporating a pinhole onto the microscope. This pinhole will reject out-of-plane scattered photons [10].

Another example of ballistic imaging is optical coherence tomography (OCT). In OCT, the interference patterns produced by the backscattered light and a reference beam are used to derive information along the axial dimension. This allows OCT to produce 3-dimensional image reconstructions with up to 1 µm spatial resolution [11]. Unfortunately, OCT can only penetrate a few mm below the surface of the tissue due to the scattering of light. As a result, OCT cannot be applied in imaging through a thick, optically-scattering human skull.

While spatial filtering and OCT have led to improvements in imaging through scattering media, multiphoton techniques are generally considered to achieve the greatest imaging depth among existing ballistic imaging techniques [12]. In this discussion, we will refer to the technology as "two-photon" microscopy, though three-photon excitation is also possible [13]. In two-photon microscopy, fluorophores are excited by two photons that are double the wavelength of excitation light in single-photon imaging. Because the excitation pulses are a longer wavelength, typically in the near-infrared regime, they can penetrate far deeper into the biological tissue. Additionally, at shallower depths, two-photon imaging is able to focus the excitation light to a single plane, thus obviating the need for a separate mechanism to reject out-of-plane

excitation [12].

Unfortunately, in all cases ballistic imaging fails beyond a limited depth penetration. This is because the number of ballistic photons decreases exponentially [2]:

$$T(x) = \exp(-\mu_s x) \tag{1.1}$$

Here, $T(x)$ is the "ballistic transmittance", or the number of ballistic photons that penetrate through a scattering media of thickness x and scattering coefficient μ_s. The scattering coefficient is a constant that can be loosely interpreted as the probability that a photon will scatter within a finite length of a scattering media [2]. The scattering coefficient is a material-dependent property.

As an example of the imfeasibility of ballistic imaging in the highly diffuse regime, consider the task of imaging through $10\,\mathrm{mm}$ of a scattering media with scattering coefficient of $\mu_s = 10\,\mathrm{mm}^{-1}$, which is a reasonable value for biological tissue [14]. In this case, the ballistic transmittance is:

$$T(10\,\mathrm{mm}) = \exp(-(10\,\mathrm{mm}^{-1})(10\,\mathrm{mm})) = \exp(-100) \approx 3.72 * 10^{-44}$$

In other words, for every $\sim 2.69 * 10^{43}$ photons emitted, on average, one will be detected. In this case, the signal would be overwhelmed by noise. Thus, ballistic imaging is impractical in the highly diffuse regime. As shown in figure 1.2, ballistic imaging technologies can generally only image through approximately 4-20 mfp [15].

1.1.2   Diffuse Optical Tomography

One technology that has gained interest for diffuse imaging is continuous-wave diffuse optical tomography (henceforth referred to as DOT). DOT is an optical imaging technique that uses an array of light sources and detectors [9]. Each detector captures an
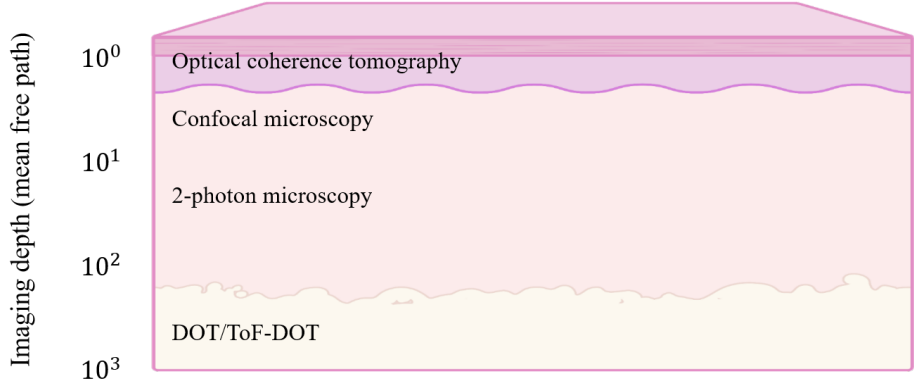
Figure 1.2 : **Imaging depth comparison:** Ballistic imaging techniques can only image shallow features. The deepest imaging is achieved by 2-photon imaging, on the order of 20 mfp. In comparison, DOT/ToF-DOT can image >100 mfp.

intensity measurement corresponding to the illumination from each source. Therefore for N_s sources and N_d detectors, we would have $N_s N_d$ total measurements. These measurements then become the input to an inverse solver, which uses a physically accurate model of light propagation, known as the forward model, to create an image reconstruction of the desired scene [8, 9]. This overall pipeline is shown in figure 1.3.
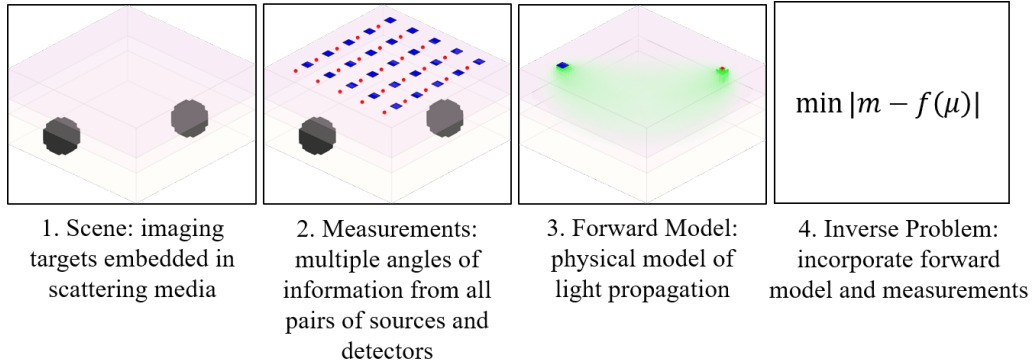
Figure 1.3 : **Overview of the DOT pipeline:** In DOT, the scene is modeled as a homogeneous scattering slab with embedded targets. To recover the target scene, a set of measurements are collected, and a forward model is established to solve the inverse problem. The key to reconstructing images through densely scattering media is a forward model that accurately represents the effects of scattering.

One of the key insights that has allowed it to achieve this imaging depth is by incorporating both ballistic and diffuse photons in its measurements [9]. Unfortunately, this increased imaging depth comes at the cost of spatial resolution. Most DOT imaging techniques achieve a spatial resolution on the order of centimeters or several millimeters. This poor spatial resolution is partially due to the densely scattering substrate, as well as the sparse number of sources and detectors that are used. The sources and detectors are often separated by several millimeters, or even centimeters [16].

Additionally, the inverse solver is often a very computationally intensive operation. This is generally due to the computational resources that are required to evaluate the forward model. Traditional DOT inverse solvers can require hours to complete a single image reconstruction [17]. Therefore, to make DOT a more feasible technology for real-time medical imaging, we must improve the spatial resolution and algorithm speeds.

1.1.3 Time-of-flight Diffuse Optical Tomography

Time of flight diffuse optical tomography (ToF-DOT) extends the ideas of DOT into the time-domain, shown in figure 1.4. In ToF-DOT, a histogram of photon arrival times is recorded at each source-detector pair [1, 18]. By introducing transient information, there is additional information that can be exploited for improved image reconstruction quality.

Additionally, time-domain information provides the ability to perform time-gating. A large amount of the noise in DOT measurements is due to short path length photons. In time-gating, early arriving photons, corresponding to the short path length photons, are rejected. This dramatically improves the signal-to-noise ratio (SNR).
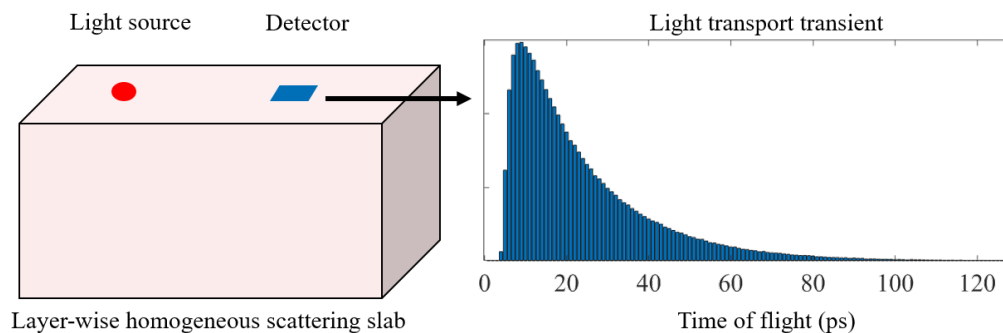
Figure 1.4 : **ToF-DOT Overview:** In time-of-flight DOT, a similar geometry can be modeled: a homogeneous scattering slab with a light source and detector placed on the surface. The primary innovation of ToF-DOT is to measure a light transport transient at each detector, rather than a scalar intensity value. This provides a greater diversity of measurements.

Unfortunately, there are numerous challenges with incorporating time-domain information. Generating time-domain measurements requires complex hardware. This leads to low fill factors and reduced sensor resolution [19]. Additionally, the greater volume of data from introducing time-domain measurements can lead to reduced data transfer rates and increased computational complexity, and therefore preclude the system from achieving a real-time response. Therefore, the focus of this thesis will be to establish techniques that improve the spatial resolution *and* the reconstruction time of ToF-DOT.

Chapter 2

DOT Forward Model and Inverse Problem

2.1 Forward Model Equations

The goal of diffuse optical tomography is to recover the spatial distribution of optical properties, i.e. to perform a 2/3D image reconstruction. To perform this image reconstruction, we must first establish an accurate forward model. The forward model determines how a specific scene, or distribution of optical parameters, leads to a corresponding set of measurements based on a physically accurate model of light propagation through the scattering media. Our ability to perform image reconstruction is largely determined based on the alignment between the experimentally captured measurements and the measurements predicted by the forward model [20]. Therefore, an accurate forward model is critical to performing high-quality image reconstructions. In this section, we present the forward model for time of flight diffuse optical tomography (ToF-DOT). Subsequently, in chapter 3, we will outline how this forward model can be adapted to GDOT.

2.1.1 Radiative Transfer Equation

The radiative transfer equation (RTE) is generally considered to be the most accurate equation for modeling light propagation in a scattering media [21, 2, 22]. The RTE assumes a particle model of light. Therefore, it does not model the effects of polarization nor coherence, which is a reasonable assumption in the highly diffuse regime.

The RTE is expressed as [2]:

$$\frac{\partial L(\vec{r}, \hat{s}, t)/c}{\partial t} = -\hat{s} \cdot \nabla L(\vec{r}, \hat{s}, t) - \mu_t L(\vec{r}, \hat{s}, t) + \mu_s \int_{4\pi} L(\vec{r}, \hat{s}', t) P(\hat{s}' \cdot \hat{s}) d\Omega' + S(\vec{r}, \hat{s}, t)$$

(2.1)

The RTE describes the distribution of light, i.e. the radiance $L()$, as a function of position, time, and solid angle, represented by the variables $\vec{r}$, t, and $\hat{s}$, respectively. The main idea represented by the RTE is the balance of energy: the changes in radiance, $\frac{\partial L(\vec{r}, \hat{s}, t)/c}{\partial t}$, is equal to the light gained minus the light lost [2]. Light is lost due to divergence and extinction, which are represented by the $\hat{s} \cdot \nabla L(\vec{r}, \hat{s}, t)$, and $\mu_t L(\vec{r}, \hat{s}, t)$ terms, respectively. Light is gained due to in-scattering and light sources, which are represented by the $\mu_s \int_{4\pi} L(\vec{r}, \hat{s}', t) P(\hat{s}' \cdot \hat{s}) d\Omega'$ and $S(\vec{r}, \hat{s}, t)$ terms, respectively.
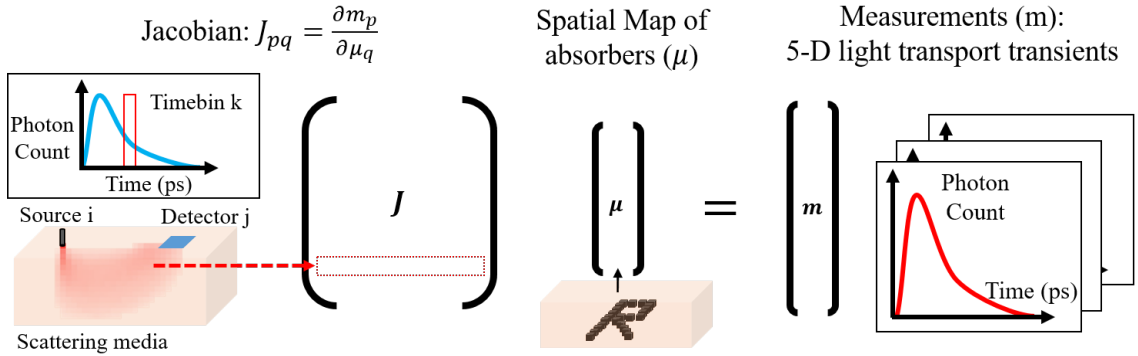
Figure 2.1 : **Forward Model:** Overview of the linear forward model for ToF-DOT. The scene (μ) is related to the measurements (m) through a linear transformation, represented by the Jacobian matrix (J).

In the form shown in equation (2.1), it is difficult to directly perform image reconstruction. To perform reconstruction, we must first determine how changes in the optical parameters lead to the set of measurements that are created. Therefore, to

establish this relationship, we use the Born Approximation. Under the Born Approximation, a linear forward relationship can be created [22, 23, 24]:

$$m = J\mu \tag{2.2}$$

Here, vector μ is the spatial distribution of absorbers. m is the set of light transport transients, our measurements. J is the Jacobian, or sensitivity matrix, which establishes a linear relationship between m and μ. The vector μ is of dimension N, where N is the number of voxels in the discretized scene. m is of dimension $Q = N_s N_d N_T$, i.e. the product of the number of sources, detectors, and time bins, respectively. Finally, the Jacobian, which is a mapping from μ to m is of dimension $Q \times N$. Figure 2.1 provides an illustration of the linear model.

The Jacobian is the key to the forward model in our image reconstructions, as it establishes a linear mapping between the set of optical parameters and the set of measurements. Formally each entry of the Jacobian is defined as the partial derivative of the measurement with respect to optical parameters: $J_{pr} = \frac{\partial m_p}{\partial \mu_r}$, i.e. what influence does a small change in the optical parameters have on the detected number of photons [22, 21]. On a high level, the Jacobian can be interpreted as the likelihood that a photon will pass through a particular point in space. If there is a greater likelihood that a photon will pass through a particular point in space, then a change in the optical parameters at that position will result in a larger change in the measurements.

In the time-of-flight measurements, the sensitivity becomes a function of time and space. This can be used to recover information on features that are embedded deeper within the scattering slab. The later time bins possess increased sensitivity to deeper features. This is because the later arriving time bins are related to photons with longer path lengths and are more likely to propagate deeper within the scattering

media. This phenomenon is shown in figure 2.2. The left side shows visualizations of the sensitivity in 3-dimensional space for different time bins. On the right, the light transport transient shows the corresponding time bins highlighted in green. We see that at early arriving time bins, there is higher sensitivity to shallower features, which are related to early arriving time bins. As we look to later time bins, the sensitivity at greater depths increases.
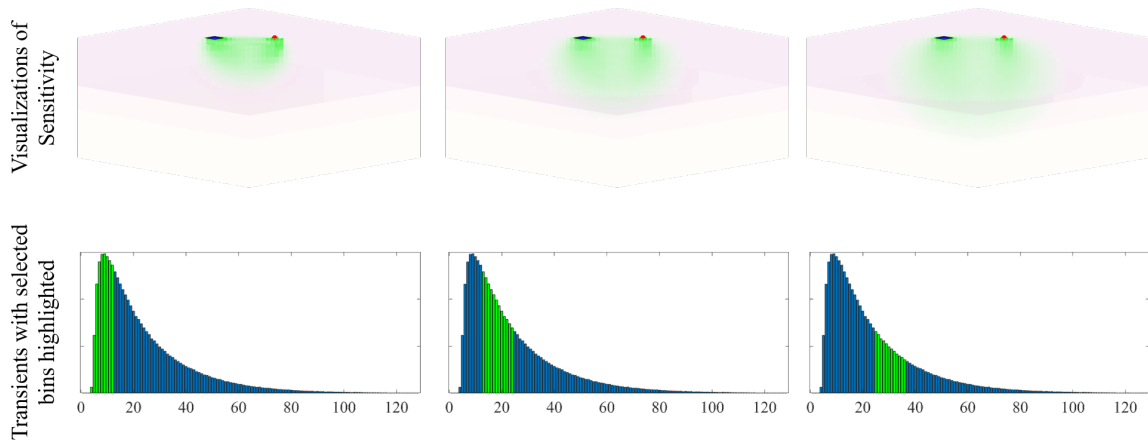
Figure 2.2 : **Visualization of sensitivity at multiple time bins:** At later time bins (i.e. longer time of flight) there is increased sensitivity to deeper features. This can aid in imaging features that are embedded deeper in an optically thick scattering media.

2.1.2   Diffusion approximation

While the RTE is an accurate and very general equation for modeling the distribution of photons, it can be mathematically challenging and computationally expensive to solve in a closed form for certain imaging geometries [2]. Therefore, a number of mathematical expressions and computational techniques have been established to approximate or estimate solutions to the radiative transfer equation.

Under certain approximations, it has been established that the RTE can be substituted for the diffusion equation (DE), using the diffusion approximation [2]. The DE can be expressed as [2]:

$$\frac{\partial \Phi(\vec{r}, t)}{c \partial t} + \mu_a \Phi(\vec{r}, t) - \nabla \cdot [D \nabla \Phi(\vec{r}, t)] = S(\vec{r}, t) \tag{2.3}$$

As shown in (2.3), the diffusion equation describes the behavior of light in terms of the fluence rate $\Phi(\vec{r}, t)$ [2]. We see that this value $\Phi(\vec{r}, t)$ is no longer a function of the solid angle $\hat{s}$. This is because, under the diffusion approximation, we assume that light now scatters isotropically. Therefore, we are no longer concerned with the scattering direction at a particular position.

The diffusion equation cannot be applied in all cases. For example, it is not appropriate to use the DE in low-scattering regimes, in which the scattering anisotropy of the photon is important, such as in regions with a small scattering coefficient [25]. However, it is appropriate in the highly scattering regime, which is often the case in diffuse optical tomography. If the DE can be applied appropriately, then it is preferable to the RTE because the problem becomes more computationally tractable.

In fact, using the diffusion approximation it is possible to directly use analytical expressions to solve the equations directly. Several prior works have shown that for simple geometries, the diffusion equation can be expressed in a closed form as [1, 3, 26]:

$$m(\vec{r}_d, \vec{r}_s) = \int_v J(\vec{r}_d, \vec{r}_s, \vec{r}_v) \mu(\vec{r}_v) d\vec{r}_v \tag{2.4}$$

$$J(\vec{r}_d, \vec{r}_s, \vec{r}_v) = \Phi_0(\vec{r}_v - \vec{r}_s, t) \circledast R(\vec{r}_d - \vec{r}_v, t) \tag{2.5}$$

In equation 2.4, the $\mu(\vec{r}_v)$, $m(\vec{r}_d, \vec{r}_s)$, $J(\vec{r}_d, \vec{r}_s, \vec{r}_v)$ terms correspond to the scene, measurements, and Jacobian, analogous to the μ, m, J terms in the linear model,

equation (2.2). From equation 2.5, we see that the Jacobian is equal to the convolution of the Green's function for the source path, $\Phi_0(\vec{r_v} - \vec{r_s}, t)$, and reflectance term, $R(\vec{r_d} - \vec{r_v}, t)$ [3, 26]. The sensitivity correspond to the probability that a photon will pass from the source at r_s to a voxel at r_v then pass from the voxel to the detector at position r_d [2]. The convolution arises as a consequence of the conditional probability.

2.1.3   Monte Carlo estimation of photon distribution

As described above, the diffusion approximation is not appropriate in all case. Therefore, as an alternative to solving the diffusion equation, it is also possible to estimate a solution for the RTE itself. This can be done using the Monte carlo (MC) algorithm. In MC, the distribution of light is estimated by averaging information from multiple photon samples. Each photon sample follows a random trajectory. This trajectory can be sampled from a distribution that is determined by the optical properties of the scattering media [1]. For each photon sample, we perform the procedure outlined in algorithm 1:

Algorithm 1: Monte Carlo procedure for each photon

---

position = [0,0,0];

dir = [0,0,1];

$\mu_a \leftarrow \mu_{a0}$;

$\mu_s \leftarrow \mu_{s0}$;

$g \leftarrow g_0$;

$n \leftarrow n_0$;

$w \leftarrow 1$;

while $in\_bounds(position)$ **do**

> position = position + $sample\_scatter\_length(\mu_a, \mu_s)$;
>
> dir = $sample\_hg$(dir, g);
>
> $w \leftarrow w\left(\frac{\mu_s}{\mu_a}\right)$;
>
> [dir, μ_a, μ_s, g, n] = $check\_layer$(position, dir, n);

According to this model, as the photon propagates, it will travel in a straight-line trajectory until it reaches a scattering-absorption event. The length of this trajectory is sampled from an exponential distribution due to the exponential falloff in the number of unscattered photons [27]. At this scattering-absorption event, the photon is scattered in a new direction. The updated direction is sampled from the Henyey-Greenstein (HG) distribution, which is an accurate model of scattering in biological tissue [28]. The HG function is a probability distribution that determines the likelihood that a photon will scatter in a particular direction. The HG function is parameterized by a value g, known as the anisotropy factor. The anisotropy factor range from 0 to 1, with higher g indicating that the material is more forward scattering. For example, a value of $g = 0$ indicates isotropic scattering (i.e. equal likelihood of scattering in any direction), and a value of $g = 1$ indicating that the photon will

continue traveling in a forward direction. Biological tissue, which is highly forward scattering, generally has an anisotropy factor of $g = 0.9$ [29].

Additionally, the weight of this photon is scaled by the albedo to account for the loss of photons due to optical absorption. This procedure is repeated until the trajectory reaches the bounds of the simulated phantom. An illustration of the Monte Carlo procedure is shown in figure 2.3. For each photon sample, we can also track its time of flight based on its propagation length. The final measurement is a histogram of the time-tagged photon samples. More details of this algorithm are described by Wang et al. [27]. The panels on the right (b-e) of figure 2.3 show simulated photons paths for increasing scattering coefficients. We see there are a larger number of scattering coefficients and less depth penetration as the scattering coefficient increases.
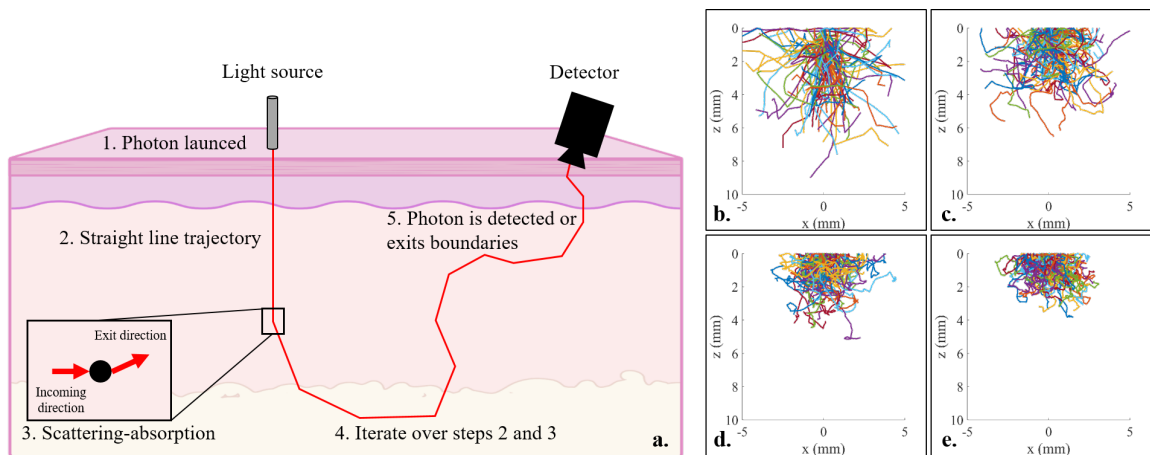
Figure 2.3 : **Monte Carlo Overview:** (a) An illustration of the procedure for the Monte Carlo algorithm for a single photon. Visualizations of simulated photon paths as the scattering coefficient increases for (b) $\mu_s = 2 \, \text{mm}^{-1}$; (c) $\mu_s = 9 \, \text{mm}^{-1}$; (d) $\mu_s = 15 \, \text{mm}^{-1}$; (e) $\mu_s = 20 \, \text{mm}^{-1}$. We see that the photon paths undergo more scattering events and are more concentrated at the surface as the scattering coefficient increases.

2.2   Fluorescence versus Absorption mode imaging

While the theory and algorithms described thus far have focused on optical absorption-based imaging targets, fluorescent targets can be modeled using a similar procedure. To image an absorbing target, we must capture a set of differential measurements. The Jacobian relates changes in the optical parameter to changes in the collected measurements. Therefore, each measurement consists of a pair of measurements: a background measurement when the target is in the unperturbed state and a target measurement when the change or perturbation has been introduced [22]. This can result in a large amount of noise. Since the ToF-DOT imaging system is typically limited by Poisson noise, the noise term is related to the intensity of the background signal. In contrast, when a fluorescent contrast agent is used, the differential measurement is the emission signal. This is because the differential measurement is equal to the number of photons that are absorbed due to the perturbation, which is directly proportional to the number of emission photons.

Finally, fluorescence contrast agents also affect the time-domain profile. There is a time delay between the instance when a photon is absorbed by a fluorophore and when it is re-released as an emission photon. This time delay can be modeled as a random variable sampled from an exponential distribution. The rate parameter of this exponential distribution is the fluorescence lifetime, which is dependent on the specific fluorophore. In the time domain, this delay can be modeled by convolving the zero-lifetime transient profile with an exponential function, parameterized by the lifetime of the fluorophore [30, 31, 32]. The zero-lifetime transient refers to the differential signal that would have been obtained if the fluorescence lifetime was zero, in other words, if there was no delay between photon absorption and re-emission.

2.2.1   Implementation using Monte Carlo

Both fluorescence and absorption-based imaging use the same iterative procedure for sampling photon trajectories, as described in algorithm 1. The differences outlined in section 2.2 can be modeled in the post-processing steps. After a time domain profile has been estimated, Poisson noise is applied. Poisson noise is applied to the simulated "background" and "target" measurements. The noisy differential measurement is the difference between these two simulated measurements. For fluorescence simulations, the Poisson noise is applied directly to the simulated differential measurement. Therefore the rate parameter is equal to the signal intensity rather than the background intensity.

Finally, since the zero-lifetime transient can be directly simulated with Monte Carlo, this transient is convolved with an exponential distribution to simulate the delay due to the fluorescence lifetime.

2.3   Solving the Inverse Problem

The inverse problem can be formulated as an optimization problem:

$$\mu' = \min_{\mu} \|f(\mu) - m\|_2 \tag{2.6}$$

Here, μ and μ' are the absorber image and reconstructed image, respectively. m is the set of measurements, and $f()$ is a function that applies the forward model. On a high level, this equation implies that we solve the inverse problem by determining the reconstructed scene, μ', that would minimize the error between the expected measurements, $f(\mu')$, and the actual measurements that were collected, m.

Using the linear forward model, the inverse problem can be set up according to

the following form [22, 33]:

$$\mu' = \min_{\mu} \|J\mu - m\|_2 + \lambda\|\mu\|_2 + \gamma\|\mu\|_1 \tag{2.7}$$

Here, $\|J\mu - m\|_2$ is the fidelity term. Additionally, we include two regularization terms: $\|\mu\|_2$ is the Tikhonov regularization term, and $\|\mu\|_1$ enforces image sparsity. λ and γ are two hyper-parameters that tune the regularization terms. Image sparsity is an acceptable assumption in this case because regions of neural activity are assumed to be sparse. Additionally, for cases in which we cannot assume image sparsity, we can instead enforce sparsity in the DCT and wavelet domain. This is done using the following term: $\|Wx\|_1$, where W is the wavelet or DCT transform [33].

Finally, equation (2.7) can be solved using a standard linear solver, such as the fast iterative shrinkage thresholding algorithm (FISTA) or the alternating direction method of multipliers (ADMM) [33, 34]. For the experimental results shown in subsequent sections, the reconstructions were done using FISTA, as it is sufficiently fast for our applications.

Chapter 3

GDOT: Gated Diffuse Optical Tomography

3.1   GDOT Overview
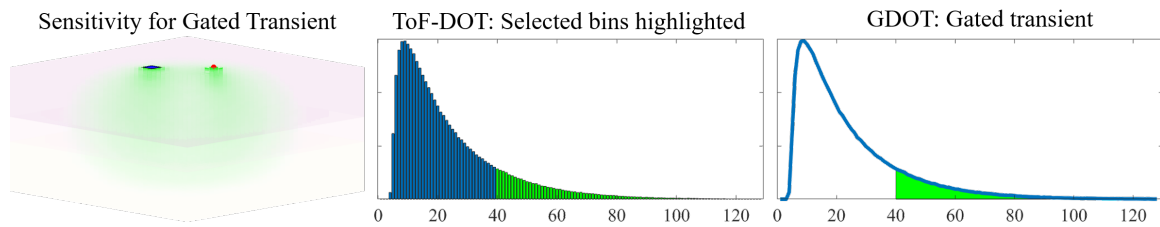
Figure 3.1 : **GDOT Introduction:** GDOT preserves the benefits of time-gating while bypassing the need to collect a full light transport transient. Instead the value recorded by each detector is a scalar.

As noted in section 1.1.3, ToF-DOT suffers from a number of challenges due to the introduction of transient information. This includes reduced sensor resolution and increased computational complexity. Both challenges can be mitigated by using time-gated measurements. For time-gated measurements, the transient is integrated from a pre-determined gate start time to the cycle limit. In this case, the measurement from each pair of sources and detectors is a scalar (figure 3.1). At the same time, the use of time-gating maintains the SNR improvements of rejecting early-arriving photons.

3.1.1   Forward model for GDOT

The forward model can be adapted from the standard ToF-DOT forward model. Recall that each entry of the measurement vector, and consequently each row of the Jacobian, corresponds to a specific source-detector-time-bin triplet. Therefore, the gated measurements can be obtained by integrating selected entries and rows of the measurement vector and Jacobian, respectively, as shown in figure 3.2. The selected entries/rows would correspond to the time bins that fall within the selected "pass-gate." This operation is a linear transform, which can be implemented in a computationally efficient manner.
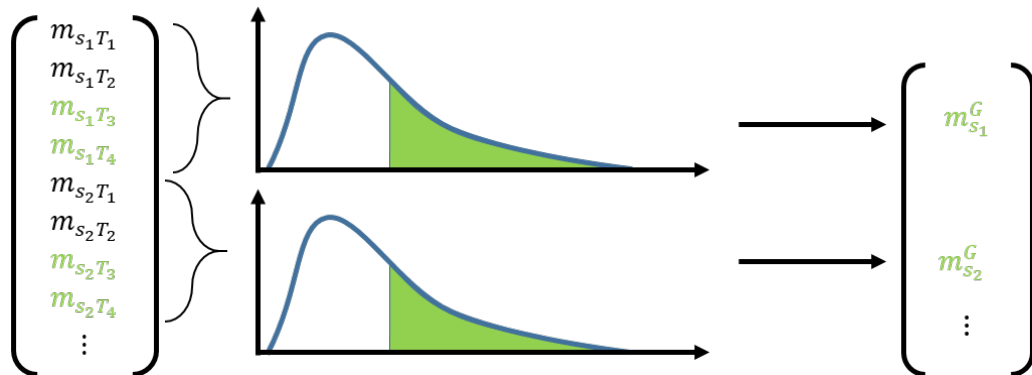
Figure 3.2 : **Forming Gated DOT Measurements:** The standard forward model described in section 2.1.1 can be applied to GDOT by summing over measurements corresponding to the "pass gate."

3.2   Confocal Geometry for GDOT

In DOT, it is common to use all pairs of sources and detectors. However, this would not be appropriate for a GDOT system because it would scale poorly as the number of sources and detectors increased. In this case, the number of measurements would be proportional to the product of the number of sources and detectors. Increasing

the size of the source-detector array from 16×16 to just 64×64 would result in a $256\times$ increase in the number of measurements.

Additionally, not all the data is equally useful for performing image reconstruction. For example, the measurement collected from a source-detector pair that is separated by a large distance (greater than a few millimeters) will be much noisier and diffuse, which will provide little information compared to nearby source-detector pairs. This is because photons will have greater sensitivity to deeper features at close source-detector separations. While close source-detector separations are typically not used in DOT due to large background noise, this can be mitigated by collecting time-domain measurements, which possess decreased sensitivity to shallower features at later time bins [35, 36].

3.2.1 Forward model for confocal geometry

The forward model in ToF-DOT outlined in section 2.1.1 uses all pairs of sources and detectors. Since the confocal geometry only uses the collocated pairs of sources and detectors, we would expect the measurements in the confocal geometry to be a subset of the set of measurements for standard ToF-DOT. For the confocal geometry, only entries of the measurement vector, which correspond to the collocated source-detector pair, are used. The Jacobian is updated in an analogous manner. Only rows of the Jacobian corresponding to the collocated pair are used since the rows of the Jacobian correspond to the entries of the measurement vector.

3.2.2 Convolutional Approximation

Next, we will show that we can apply a convolutional approximation for the confocal geometry. From our analysis in section 2.1.1 we have already shown that the forward

model can be represented as a linear system. Therefore, what remains is to demonstrate that the system is shift-invariant. In figure 3.3, we see a visualization of rows of the Jacobian. The scene consists of a $32 \times 32 \times 1$ array of voxels. From the 1-dimensional profiles, we see that the profile for each row of the Jacobian is the same, albeit shifted. Additionally, this shift corresponds to the shift in the source-detector pair. Thus, we have demonstrated in simulation that the system is shift-invariant, and therefore applying the forward model can be approximated by a convolution.
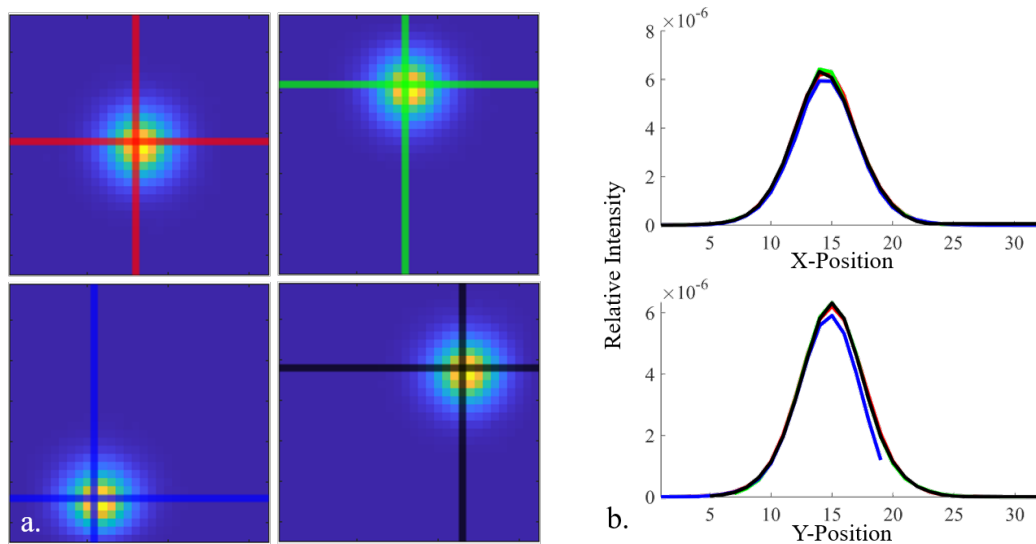
Figure 3.3 : **Confocal GDOT Shift-Invariance:** (a) visualization of rows of the Jacobian for the confocal geometry (b) X and Y slices, showing that the profiles in the rows of the Jacobian are approximately the same, but shifted in space. Combined with the linearity assumption, we can therefore apply a convolutional approximation.

The convolutional approximation can be used to achieve greater speed-ups in the reconstruction algorithm. Most algorithms that solve linear inverse problems require the forward model to be applied repeatedly. Repeatedly calculating a matrix-vector multiplication can become very computationally expensive, particularly when the Jacobian matrix grows large. Alternatively, the convolutional approximation can be

efficiently implemented using the fast Fourier transform (FFT). To see the improvements in the convolutional approximation, we consider an $M \times M$ array of sources and detectors, T time bins per transient measurement, and a target scene consisting of $M \times M$ voxels. In this case, the Jacobian would be of size $TM^4 \times M^2$, resulting in a computational complexity of $\mathcal{O}(TM^6)$. In contrast, the convolutional approximation, using the FFT, achieves a computational complexity of $\mathcal{O}(TM^2 \log(M))$.

The point spread function (PSF) that is used in the convolutional model can be simulated using the Monte Carlo algorithm. To recover the PSF, we must simulate the impulse response. The most straightforward way to obtain the impulse response is to obtain a full set of measurements for a single absorber, analogous to an optical delta function. Since the run time of the Monte Carlo simulation is proportional to the number of light sources that are simulated, a faster approach to obtaining the PSF is by determining a row of the Jacobian: simulate a single source-detector pair and a voxel array corresponding to the desired PSF dimensions.

As it is currently described, the convolutional approximation requires the target scene to be fixed to a specific depth. This requires a two-dimensional convolution. To obtain depth information, this two-dimensional convolution can be applied over multiple depths. However, this does not allow for an efficient 3-dimensional convolutional approximation because the relationship between the depth dimension of the scene and the time dimension of the measurements cannot be approximated by a convolution. Extending the convolutional approximation to three-dimensional convolutions will be further explored in future work. One alternative to producing three-dimensional image reconstructions is to utilize the full Jacobian. While this sacrifices the computational efficiency of the convolutional approximation, it allows for three-dimensional reconstruction.

Chapter 4

Materials and Methods

4.1   Simulation Methods

An in-house Monte Carlo simulator was created to generate both the simulated measurements, which are used in the performance characterization, as well as the Jacobian matrix, which is used for image reconstruction on both simulated and experimental data. All Monte Carlo algorithms were implemented in CUDA C++ and run on a server that hosted 8 Nvidia 2080Ti GPUs.

The traditional Monte Carlo algorithm described by Wang et al. is highly amenable to parallelization [27]. This is because each photon sample requires a large number of arithmetic calculations to sample a random trajectory; however, it uses very little memory, storing only its position, direction, and the photon "weight." In contrast, the Jacobian matrix typically requires a much larger amount of memory because each photon sample must now store information regarding its interaction with every voxel along its trajectory. To address this challenge, we implemented a version of the photon replay algorithm described by Yao et al. [22]. Because the efficient estimation of the Jacobian is essential to the subsequent image reconstruction algorithm, we summarize the approach of Yao et al. as follows [22]:

The key insight of this algorithm is that only a small fraction of simulated photons will pass from the source to the detector. It would be computationally wasteful to allocate blocks of memory for the photon to store data on its interaction with voxels,

only for the sample to be tossed out because it did not reach the detector. To address this, a two-step procedure is used. First, a standard Monte Carlo simulation is performed to determine which photon trajectories will reach the detector, i.e. which are the "successful" paths. The random seeds for these "successful" paths are stored. Second, another Monte Carlo simulation is run, using only the random seeds of the "successful" paths, which results in the same photon trajectory. As a result, the memory-intensive simulations, which require the GPU to store information regarding the interaction of the photon with each voxel, are run for *only* paths that reach the detector. In this way, the Jacobian can be efficiently estimated on a GPU, using the Monte Carlo algorithm.

Simulated measurements were generated by applying the forward model to a simulated scene. A simulated scene consisted of a 2/3-dimensional array representing a voxel grid. The simulated scene was assumed to be binary, and so each entry took on either a value of 0 or μ_a, representing the absorption coefficient. The forward model can then be applied. If the standard forward model is used, then the array representing the scene is vectorized and multiplied with the Jacobian matrix to obtain the set of ground truth measurements. If the convolutional approximation is applied, then the ground truth measurements are obtained through a 2-dimensional convolution between the ground truth scene and the simulated point spread function for each time bin. Finally, noise is applied to the simulated ground truth measurements. Because our system is shot noise limited, we apply Poisson noise to the measurements.

Additionally, the analytical expressions described in section 2.1.2 were used in certain performance analysis experiments. This is because these experiments require the generation of a large number of Jacobians, which can be done more efficiently using analytical expressions. The assumptions of the diffusion approximation are

appropriate here because a densely scattering slab (thickness of $6.5\,\mathrm{mm}$, $\mu_s = 9\,\mathrm{mm}^{-1}$) is used. All computational experiments, except the Monte Carlo simulations, were run on an Intel Xeon E-2136 3.30 GHz CPU. This includes evaluating the analytical expressions and running the inverse solver.

4.2   Experimental Methods

While an eventual ToF-DOT imaging system would utilize an integrated array of light sources and detectors, such a technology is still under development. Thus, to test the capabilities of the proposed system under real-world conditions, we constructed an experimental prototype. Our prototype system consists of several components. A single-pixel single-photon avalanche diode (SPAD) is used to detect photons. For our system, we use the MPD FastGatedSPAD. A Picoquant Hydraharp 400 is used as the time-correlated single-photon counter (TCSPC) for the timestamping and histogramming hardware. An MPD Picosecond Delayer (PSD) is used to control the gate rise time for hardware-based time gating. Finally, an NKT Supercontinuum laser provides the light source.

To emulate the effect of an array of sources and detectors, the single-pixel detector and the laser beam path are steered using a pair of galvo mirrors (Thorlabs GVS012), as shown in Fig. 4.1. A checkerboard calibration procedure is used to map the galvo mirror settings to points on the imaging target. The details of this procedure are described in [37].

4.2.1   Imaging Target

The imaging targets are also a key component of the imaging system. Since the ultimate target of our imaging system is for biomedical applications, we test the
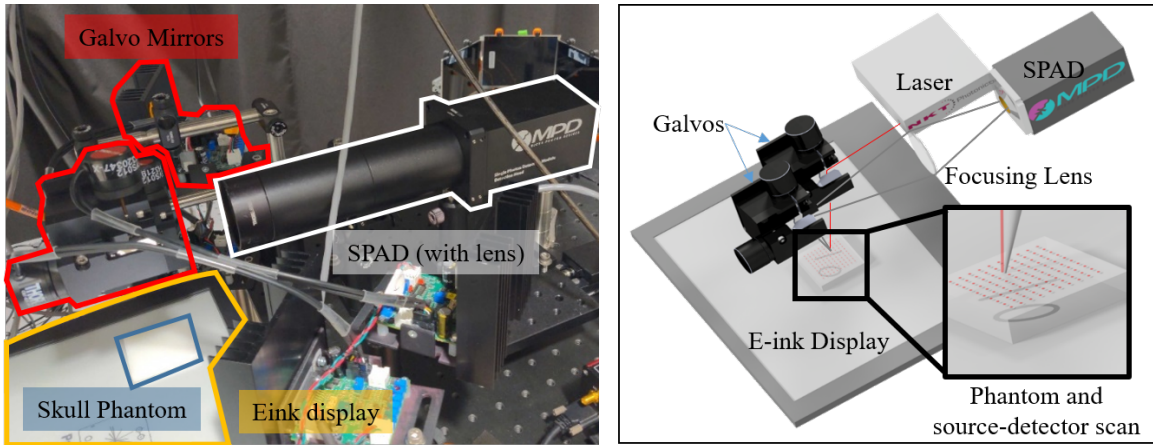
Figure 4.1 : **Experimental Setup:** An image of the experimental setup is shown above. The MPD SPAD is outlined in white. The single-pixel detector and laser beam are steered by a pair of galvos (red outline). The Eink display is outlined in orange. Placed above it is the skull phantom (blue outline). On the right, we show a rendering of the same experimental setup (rendering courtesy of Ankit Raghuram).

system on tissue phantoms that mimic the relevant optical properties of true biological tissue.

Electronic Ink Display: The imaging target consists of an Eink display, the Dasung Paperlike 3. Rather than tuning the color and brightness of an array of light sources, Eink displays images by tuning the optical scattering and absorption properties at different locations along the screen, i.e. tuning the grayscale levels [38]. This makes the Eink display an ideal imaging target because the spatial distribution of absorbers and scatterers can be programmatically controlled. The primary limitation of the Eink display is that the imaging target is constrained to a fixed depth. However, the models described in section 2.1 can naturally be extended from 2-dimensions to 3-dimensions by changing the dimensionality of the sensitivity matrix. In future work, we plan to demonstrate our ability to image on 3D targets.

Scattering tissue phantom: Additionally, our tissue phantoms are synthesized

in-house. These tissue phantoms mimic the relevant optical properties of biological tissue. Since tissue is heavily dominated by optical scattering, we focus on synthesizing and characterizing phantoms with the correct scattering properties.
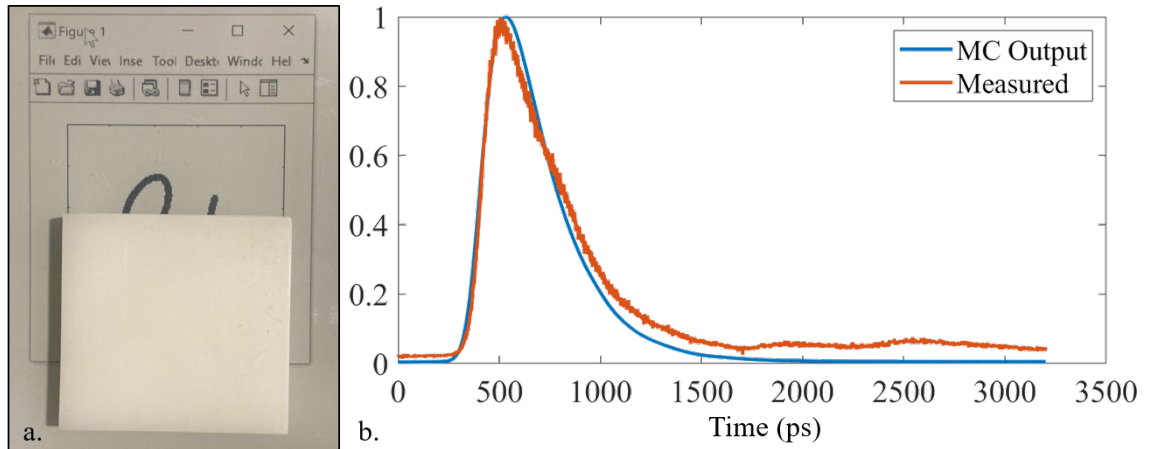
Figure 4.2 : **Optical Phantom Calibration:** (a.) Image of the synthesized tissue phantom obscuring the imaging target, which is displayed on the Eink display (b.) Simulated (blue) and experimentally captured (orange) TPSF for a scattering slab in transmission geometry. The results show good agreement between the 3D printed and simulated phantoms with $\mu_s = 9\,\text{mm}^{-1}$.

Our tissue phantoms are synthesized using a Formlabs Form 3 printer. Our procedure is adapted from the synthesis technique described by Dempsey et al [39]. We can control the optical scattering properties of the resulting tissue phantom by tuning the relative volumes of the Form clear and white resins, which, as the names suggest, are optically transparent and scattering, respectively. Rather than establishing a mathematical relationship between the concentrations of the resins and the scattering properties, we establish an empirical relationship by directly measuring the optical scattering properties. This procedure is described by Bouchard et al. [40]. The key idea is that optical scattering and absorption cause changes in the temporal point spread function (TPSF). More specifically, as the scattering coefficient

increases, there is a broadening of the TPSF. Therefore, the scattering coefficient can be experimentally determined by fitting the simulated and experimental TPSF. Figure 4.2 shows good agreement between the experimental and simulated TPSF. Also, note that we convolve the simulated TPSF with an experimentally measured instrument response function (IRF) to account for temporal broadening from the imaging system.

In conclusion, our imaging hardware consists of a laser and a single-pixel time-of-flight imaging system. Our system uses galvo mirrors to raster scan the scene. The scene is composed of a scattering tissue phantom, which is placed on top of an Eink display that displays the target. Finally, our Monte Carlo simulator is capable of generating both simulated measurements and the forward model that is needed for image reconstruction on experimental data.

Chapter 5

Performance Characterization and Analysis

We want to gauge how the imaging system performs under various imaging settings. This performance characterization is performed using simulations. We specifically test four parameters, which are the algorithm runtime, the conditioning of the Jacobian matrix, the optimal gating position, and the spatial resolution of the system.

5.1 Jacobian Matrix Conditioning
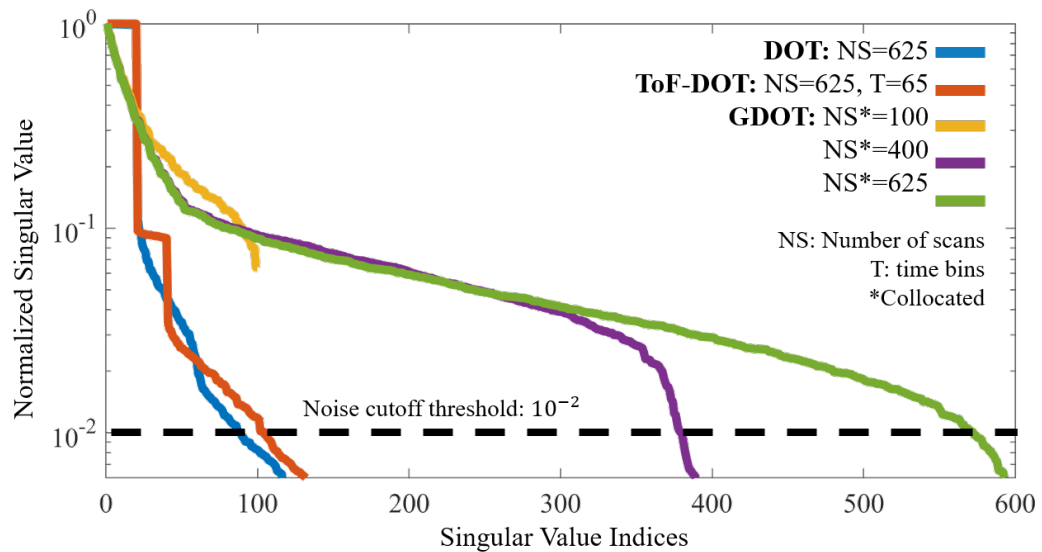
Figure 5.1 : **Singular Value Falloff:** Singular value decomposition for DOT, ToF-DOT and GDOT at multiple scan resolutions. For DOT and ToF-DOT different source-detector pair separations were used, while for GDOT only collocated source-detector pairs were used. We see that GDOT has a better conditioned Jacobian matrix.

In our linear model, inverting the Jacobian matrix is the key to performing image reconstruction. Therefore, it is important to characterize how well-conditioned the Jacobian is to determine our ability to invert the Jacobian and solve the inverse problem. Here, we characterize the Jacobian matrix based on the falloff of its singular values. Though the DOT, ToF-DOT, and GDOT systems all use the same number of measurements, GDOT performs the best. This is because GDOT uses only collocated measurements, while DOT and ToF-DOT use measurements from sources and detectors at multiple positions, which leads to measurements from multiple source-detector separations. This suggests that our GDOT system, using a confocal geometry, can achieve better image reconstruction quality.

5.2   Simulated Resolution Test

The spatial resolution establishes the minimum feature size that can be resolved by our imaging system. One method for characterizing the spatial resolution is to determine the minimum separation distance at which two features, usually two lines or two point sources, can be resolved as distinct features [18]. However, a binary output, which determines whether two features are resolved or unresolved, may not be a satisfactory output. As we can see in figure 5.2, in certain cases, the output may not show two fully fused features, nor does it show two fully distinct peaks.

In our simulated experiments, we characterize the spatial resolution based on the modulation transfer function (MTF) [41]. The ground truth images consist of a series of lines with a specific spacing. A set of measurements and image reconstruction are simulated for each ground truth image. For each line spacing, a value between 0 and

1 can be calculated using the following equation [41]:

$$M = \frac{A_{\text{max}} - A_{\text{min}}}{A_{\text{max}} + A_{\text{min}}} \tag{5.1}$$

This value measures how well our system can resolve the series of lines. We can see that as M goes to zero as the lines become fused together (i.e. the regions that should be high and low intensity have the same intensity). Conversely, as M goes to one, we are perfectly able to resolve between the high and low intensities. We see that this function establishes a relationship between the line spacing, i.e. the spatial frequency, and the system's ability to resolve fine features, hence the name "modulation transfer function."
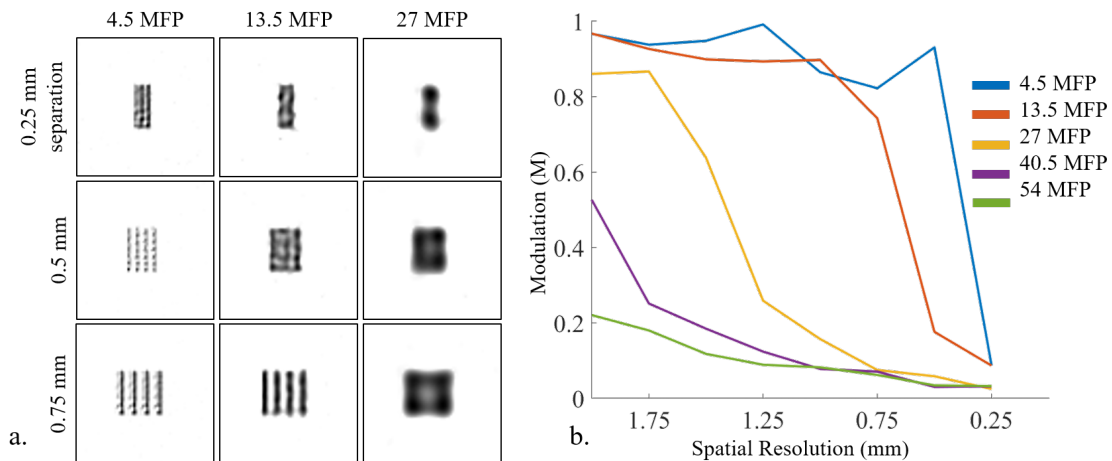
Figure 5.2 : **Simulated Resolution Test:** The modulation transfer function (MTF) provides a means of quantifying the spatial resolution as a value between 0 and 1. (a) Image reconstructions of a series of lines with varying thicknesses and increasing scattering thickness. (b) Plots of the MTF as a function of spatial resolution for multiple scattering thicknesses.

In Figure 5.2, we show plots of the MTF for various scattering thicknesses. As expected, the system performance degrades as the scattering thickness increases.

5.3   Algorithm Runtime

One of the primary objectives for implementing confocal GDOT was to reduce the runtime for the reconstruction algorithms. Therefore we test the image reconstruction speeds for confocal GDOT and compare it to the runtime for DOT and ToF-DOT reconstruction. To perform this characterization, we implemented in-house versions of the forward model for the DOT and ToF-DOT algorithms described by Wang et al and Hyde et al, respectively [2, 3]. We then timed the inverse solver using each of these three forward models: DOT, ToF-DOT, and GDOT. To establish a fair comparison across the three different techniques, we use the FISTA algorithm for all three approaches and run 100 iterations for each forward model.
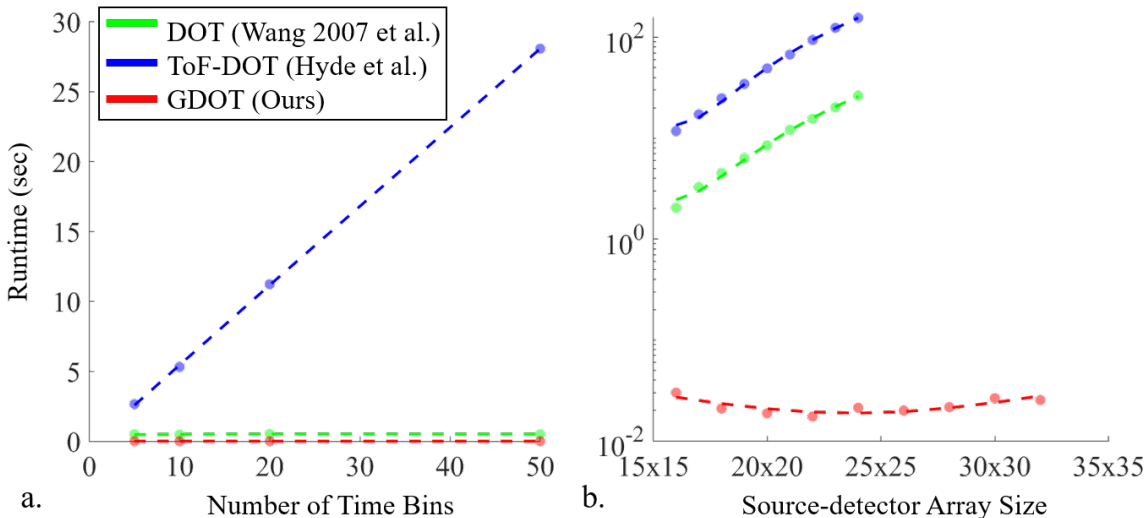
Figure 5.3 : **Algorithm Runtime Tests:** We compare the run time of the GDOT algorithm with in-house implementations of standard DOT and ToF-DOT algorithms [2, 3]. We tested the runtime as we vary (a) the number of time bins and (b) the dimensions of the source-detector array.

Additionally, for each algorithm, we test the reconstruction time as certain scene parameters are varied. In particular, the parameters of interest include the number

of time bins, the number of sources, the number of detectors, and the size of the voxel array that represents the scene.

5.4   Optimal Gating

Finally, it is essential to determine the optimal start time for the time gate. On a high level, if the gate start time is too early, then the background noise will be very large; conversely, if the gate start time is too late, then too much of the signal itself will be rejected by the time gate. This intuition can be formalized by analyzing the signal-to-noise ratio (SNR) as a function of the gate start time.

The various sources of noise include dark count noise, shot noise, and background noise. Dark noise is due to the sensing electronics, which may log a count, even in the absence of a detected photon. Dark noise can be modeled as a Poisson random variable with a rate parameter that is based on the hardware. Typically this value is characterized and documented for the specific SPAD. For the FastGatedSPAD this value is 200 counts per second [42]. This is the only source of noise that is independent of both the signal and background intensity.

Shot noise is also present in our system. This value is a Poisson random variable with a rate parameter equal to the signal intensity. Finally, background noise must also be accounted for. This noise can also be modeled as a Poisson random variable; however, it is dependent on the intensity of the background intensity rather than the signal intensity. In determining the optimal gate start time, we focus on optimizing the signal to background ratio because this is the dominant source of noise in our system.
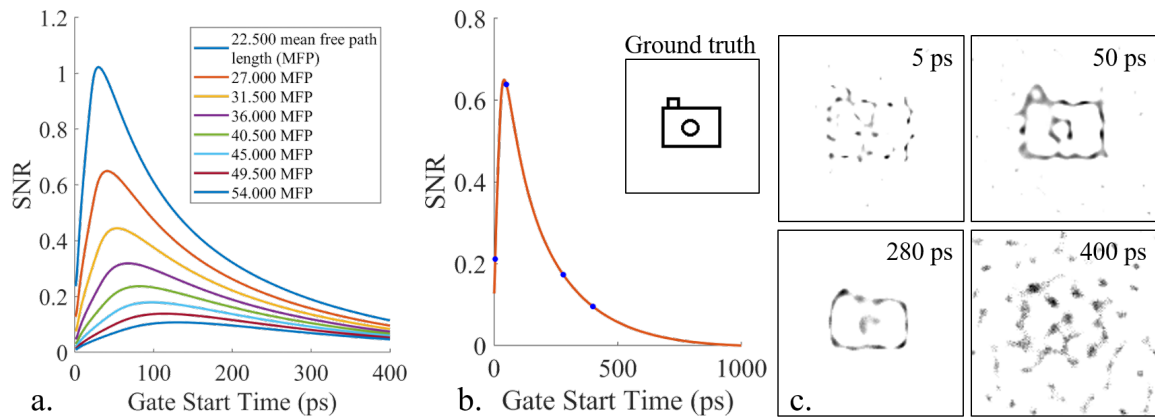
Figure 5.4 : **Optimal Gating:** In simulation, we determine the optimal gate start time by optimizing the signal-to-noise ratio (SNR). (a) The plot of SNR versus the gate start time across different optical thicknesses; (b) the SNR vs gate start specifically for 27 mfp; (c) the image reconstructions for multiple gate start times.

Chapter 6

Experimental Results

Finally, we test our results on experimental data, which was collected with our prototype setup. For most of these experiments, the test target consisted of an Eink display with a skull phantom of variable thickness placed in front of the target. The primary exception is the fluorescent imaging target. For these targets, the tissue phantoms consisted of a PDMS base with the fluorescent feature embedded in the substrate.

In these experiments, our primary aim is the following:

1. Compare GDOT to existing techniques for imaging through scattering media

2. Test the performance of GDOT at a variety of optical thicknesses

3. Demonstrate that GDOT can be applied for both absorption-mode and fluorescence-mode imaging

6.1 Comparison of multiple imaging techniques

We first tested imaging through a tissue phantom, which mimics all the relevant optical properties of the human skull. The details of this synthesis procedure are described in section 4.2.1. There is no single value that can be used for the scattering coefficient and physical thickness of all human skulls, as this will vary from person to person and even across different regions of the skull for the same person [43]. However, we chose values that are considered to be within the acceptable range in

the literature. For this experiment, we used a scattering coefficient of $\mu_s = 9\,\mathrm{mm}^{-1}$, and a physical thickness of $6.5\,\mathrm{mm}$, which are values that are considered within the reasonable range [14, 43]. The $6.5\,\mathrm{mm}$ physical thickness corresponds to an optical thickness of ~ 60 mfp.

Using this skull phantom, we tested the image reconstruction quality over several imaging methods. This included widefield microscopy, diffuse optical tomography (DOT), time-of-flight diffuse optical tomography (ToF-DOT), and gated diffuse optical tomography (GDOT). Additionally, we imaged on multiple ground truth targets, including the letter R, a circle and a line, and a pattern mimicking a vasculature structure. The results of this image reconstruction procedure are shown in figure 6.1.

We see that the widefield images fail to resolve any features due to the optical thickness of the skull phantom. The DOT and ToF-DOT images were captured with a sparse source-detector array scan of 8×8 source-detector pairs, using measurements from all pairs of sources and detectors in the array. For GDOT, we used a dense scan of 32×32 sources and detectors. We see that all three imaging modalities are able to resolve the main features of the respective images. GDOT appears to achieve the highest image reconstruction quality in this case. Additionally, in this case, the ToF-DOT image reconstructions use the temporal filters described by [44]. For this reason, the ToF-DOT image reconstructions could still achieve further improvements. This will be left for future work.

6.2   High-resolution GDOT

One of the primary benefits of GDOT is the ability to use a higher-resolution array of sources and detectors. To showcase this benefit, we also tested image reconstruction through optically thinner skull phantoms. In figure 6.2., we see the results of per-

Ground Truth	Widefield	DOT 8x8	ToF-DOT 8x8	GDOT 32x32
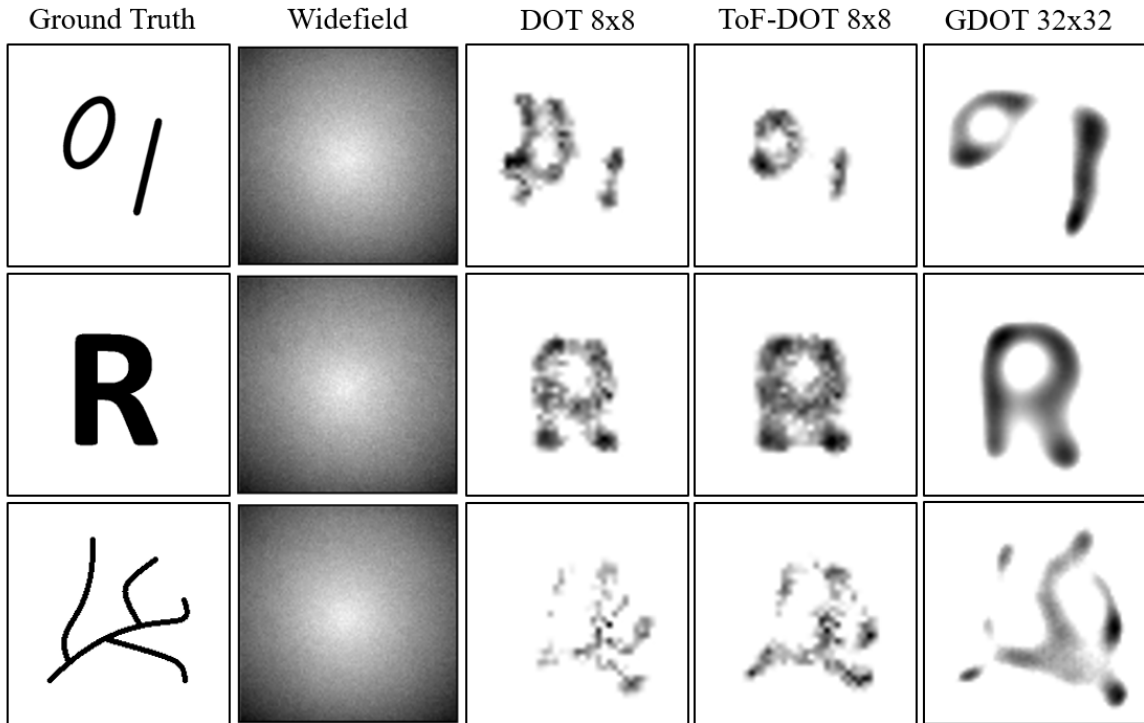
Figure 6.1 : **Imaging through skull phantom:** Above, we show the results of imaging through a 6.5 mm ($\sim$ 60mfp) tissue phantom. The ground truth targets are shown in column one. The reconstructions using different techniques are shown in subsequent columns: widefield, DOT with an 8×8 source-detector array, ToF-DOT with an 8×8 source-detector array, and GDOT with a 32×32 source-detector array

forming image reconstruction through a 9 mfp optically thick phantom. The ground truth target is the Rice owl. For this image reconstruction, a source-detector array of size 128×128 was used. We see that GDOT is able to resolve the fine features and thin lines that are present in the Rice owl image.

Additionally, we tested the image reconstruction quality at several imaging depths. The same ground truth image was used for all image reconstructions: a vasculature pattern consisting of three different line thicknesses: 2 mm, 1 mm, and 0.5 mm. We tested the image reconstruction quality at optical thicknesses of 9, 27, 36, 45, and 58.5 mfp. Finally, we also compared the image reconstruction quality of GDOT against
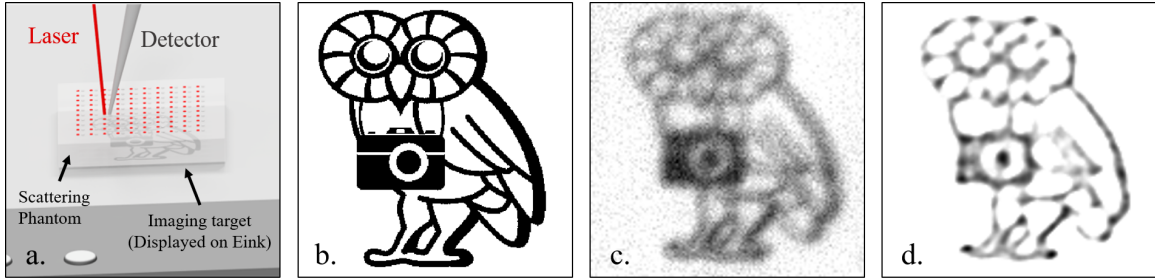
Figure 6.2 : **Image reconstruction with high-resolution detector:** (a) Rendering of the scan procedure (rendering courtesy of Ankit Raghuram); (b) Ground truth image of the Rice owl; (c) Raw measurements; (d) Image reconstruction. At reduced optical thicknesses, using a higher resolution GDOT source-detector array allows us to achieve higher-resolution image reconstruction.

DOT and ToF-DOT, as well as testing a variety of scan resolutions for GDOT at each optical thickness. The DOT and ToF-DOT image reconstructions used an 8×8 source-detector array. The size of the GDOT source-detector array varied from 16 to 64. The results of this experiment are shown in figure 6.3.

We see that GDOT generally achieves the highest image reconstruction quality at each imaging depth. Particularly at shallower imaging depths, a higher resolution source-detector array is necessary for constructing high-quality image reconstructions. Additionally, GDOT is still capable of achieving relatively high-quality image reconstructions at higher optical thicknesses. This demonstrates that GDOT is also a flexible technology, which can be applied to imaging at a variety of optical thicknesses and consequently can be targetted for multiple applications.

6.3 Fluorescence imaging

Finally, to demonstrate the flexibility of the GDOT system, we show that GDOT can image fluorescence image targets, in addition to imaging optical-absorption-based
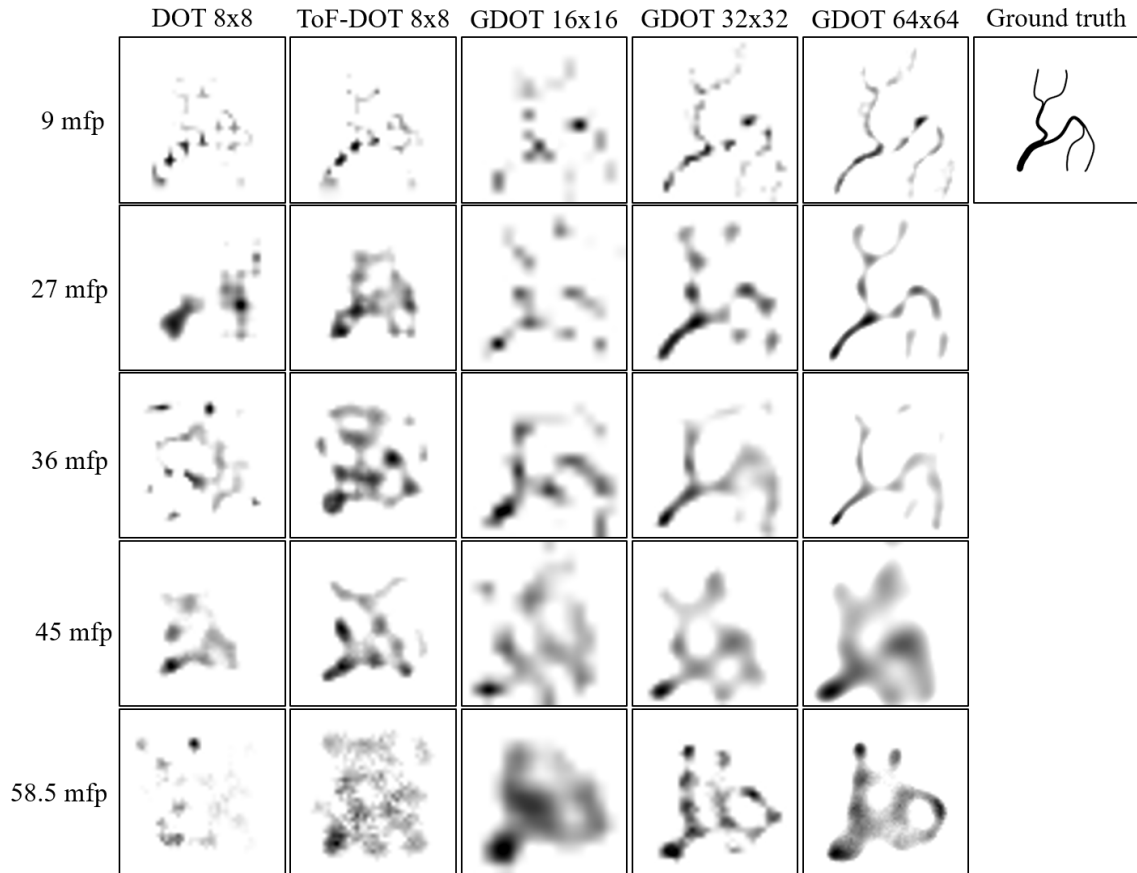
Figure 6.3 : **Image reconstruction for multiple optical thicknesses and scan resolution:** Using a finer scan resolution, GDOT achieves improved image reconstruction quality at multiple imaging depths.

imaging targets. Time gating is particularly effective for fluorescence imaging because the fluorescence lifetime increases the signal intensity at later time of arrival, at which time the background signal has been significantly reduced.

In figure 6.4, we see an image reconstruction performed for the "circle and line" target scene. Here, the fluorophores were embedded in a PDMS substrate. A source-detector array of size 32×32 was used. These measurements were captured using a confocal geometry rather than collecting measurements from all pairs of sources and detectors. In this experiment, a hardware-based time-gate was applied. Therefore,

the measurements were directly captured in gated mode.
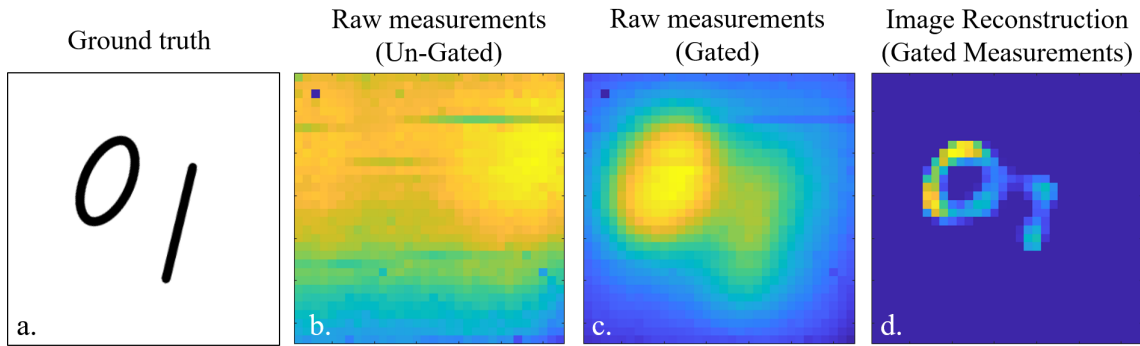
Figure 6.4 : **Fluorescence Image Reconstruction:** (a) ground truth image; (b) noisy raw measurement in free-running (un-gated) mode; (c) gated measurements show clearer image of underlying feature; (d) reconstructed circline line using time-gated measurements. We see that time-gating significantly improves the SNR of time-gated measurements.

From this result, we see that fluorescence imaging highly benefits from time-gating, which can remove a significant portion of the background noise from the excitation light. In panel b, we see that the un-gated measurement is overwhelmed by the background noise. Consequently, this would result in poor image reconstruction. However, after a time-gate is applied, the signal-to-noise ratio is significantly increased (panel c), and the image reconstruction shows good alignment with the ground truth (panel d).

Chapter 7

Discussion and Conclusion

7.1 Future Work

Two of the principal challenges that remain in this work are to extend the image reconstructions to 3-dimensional reconstructions, as well as to perform image reconstruction on in-vivo test subjects. With regards to 3-dimensional reconstruction, one of the principal challenges is the technical challenges associated with synthesizing a 3-dimensional tissue phantom. This challenge can be resolved using 3D printing to generate targets with an embedded vasculature structure. With regards to the algorithms, as noted in section 3.2.2, 3-dimensional reconstructions can be achieved directly using the Jacobian matrix with a confocal geometry.

Additionally, another future goal of GDOT is to test on in-vivo test subjects. One of the primary challenges for transitioning from tissue phantoms to in-vivo test subjects is the reduced contrast and increased background noise in a biological sample. Imaging under these conditions would require algorithms that are robust to reduced SNR. In this case, machine learning methods may be promising. Such algorithms would likely be trained on simulated data to provide sufficient training examples.

7.2 Conclusion

Optical imaging is a promising avenue for developing novel brain-computer interfaces, as it is safe for users and can be built into a compact, wearable devices. Due to the

effects of optical scattering, diffuse optical tomography and its time-domain variant, time-of-flight diffuse optical tomography, are two of the few existing technologies that can image through densely scattering biological tissue, in particular the human skull. In this work, we present a novel technology, which we have coined gated diffuse optical tomography (GDOT), which advances these existing technologies. In particular, GDOT uses only time-gating and does not require the imaging system to capture full light transport transients. As a result, GDOT retains the benefit of an increased signal-to-noise ratio from rejecting early-arriving background photons using time-gating. At the same time, GDOT is able to reduce the amount of data that must be transferred and processed and utilizes a higher resolution detector. This simultaneously increases the spatial resolution at various optical depths and decreases the run time of the associated image reconstruction algorithms. In simulation, we conducted a performance analysis. We demonstrated the superior algorithm run time of GDOT, demonstrated that GDOT could achieve mm-scale spatial resolution for imaging at optical thicknesses that are appropriate for biological tissue, tested the conditioning of the sensitivity matrix, and finally characterized the optimal time-gate start time. In addition, we constructed an experimental prototype consisting of a single-pixel detector, a pulsed laser, and a pair of galvo mirrors to raster-scan the source and virtual detector at different points on the imaging target. Using experimental data collected from this prototype system, we tested our image reconstruction algorithms. We determined that our system achieves a superior image reconstruction quality compared to traditional optical imaging techniques, including DOT, ToF-DOT, and widefield imaging. In our future work, we will extend our system to imaging 3-dimensional imaging targets and eventually test on in-vivo test subjects.

Bibliography

[1] Y. Zhao, A. Raghuram, H. Kim, A. Hielscher, J. T. Robinson, and A. N. Veer-araghavan, "High resolution, deep imaging using confocal time-of-flight diffuse optical tomography," *IEEE Transactions on Pattern Analysis and Machine Intelligence*, 2021.

[2] L. Wang and H.-I. Wu, *Biomedical Optics: Principles and Imaging.* Hoboken, NJ: John Wiley and Sons, 2007.

[3] D. Hyde, *Improving Forward Matrix Generation and Utilization for Time Domain Difiuse Optical Tomography.* PhD thesis, Worcester Polytechnic Institute, 2002.

[4] E. C. Leuthardt, G. Schalk, J. Roland, A. Rouse, and D. W. Moran, "Evolution of brain-computer interfaces: going beyond classic motor physiology," *Neurosurgical Focus FOC*, vol. 27, no. 1, p. E4, 01 Jul. 2009.

[5] J. J. Shih, D. J. Krusienski, and J. R. Wolpaw, "Brain-computer interfaces in medicine," *Mayo Clinic proceedings*, vol. 87, pp. 268–279, mar 2012.

[6] L. Jiang, A. Stocco, D. M. Losey, J. A. Abernethy, C. S. Prat, and R. P. N. Rao, "BrainNet: A Multi-Person Brain-to-Brain Interface for Direct Collaboration Between Brains," *Scientific Reports*, vol. 9, no. 1, p. 6115, 2019.

[7] K. Kay, K. W. Jamison, L. Vizioli, R. Zhang, E. Margalit, and K. Ugurbil, "A

critical assessment of data quality and venous effects in sub-millimeter fMRI.," *NeuroImage*, vol. 189, pp. 847–869, apr 2019.

[8] A. H. Hielscher, A. Y. Bluestone, G. S. Abdoulaev, A. D. Klose, J. Lasker, M. Stewart, U. Netz, and J. Beuthan, "Near-infrared diffuse optical tomography.," *Disease markers*, vol. 18, no. 5-6, pp. 313–337, 2002.

[9] D. A. Boas, D. H. Brooks, E. L. Miller, C. A. DiMarzio, M. Kilmer, R. J. Gaudette, and Q. Zhang, "Imaging the body with diffuse optical tomography," *IEEE signal processing magazine*, vol. 18, no. 6, pp. 57–75, 2001.

[10] M. Minsky, "Microscopy apparatus," U.S. Patent 3013467A, Nov. 1957.

[11] J. G. Fujimoto, C. Pitris, S. A. Boppart, and M. E. Brezinski, "Optical coherence tomography: an emerging technology for biomedical imaging and optical biopsy," *Neoplasia (New York, N.Y.)*, vol. 2, no. 1-2, pp. 9–25, 2000.

[12] R. K. P. Benninger and D. W. Piston, "Two-photon excitation microscopy for the study of living cells and tissues," *Current protocols in cell biology*, vol. Chapter 4, pp. Unit–4.11.24, jun 2013.

[13] N. G. Horton, K. Wang, D. Kobat, C. G. Clark, F. W. Wise, C. B. Schaffer, and C. Xu, "In vivo three-photon microscopy of subcortical structures within an intact mouse brain," *Nature Photonics*, vol. 7, no. 3, pp. 205–209, 2013.

[14] F. Bevilacqua, D. Piguet, P. Marquet, J. D. Gross, B. J. Tromberg, and C. Depeursinge, "In vivo local determination of tissue optical properties: applications to human brain," *Applied Optics*, vol. 38, no. 22, pp. 4939–4950, 1999.

[15] A. K. Pediredla, S. Zhang, B. Avants, F. Ye, S. Nagayama, Z. Chen, C. Kemere, J. T. Robinson, and A. Veeraraghavan, "Deep imaging in scattering media with selective plane illumination microscopy," *Journal of Biomedical Optics*, vol. 21, no. 12, pp. 1–14, 2016.

[16] M. D. Wheelock, J. P. Culver, and A. T. Eggebrecht, "High-density diffuse optical tomography for imaging human brain function," *Review of Scientific Instruments*, vol. 90, p. 51101, may 2019.

[17] H. K. Kim and A. H. Hielscher, "A PDE-constrained SQP algorithm for optical tomography based on the frequency-domain equation of radiative transfer," *Inverse Problems*, vol. 25, no. 1, p. 15010, 2008.

[18] A. Lyons, F. Tonolini, A. Boccolini, A. Repetti, R. Henderson, Y. Wiaux, and D. Faccio, "Computational time-of-flight diffuse optical tomography," *Nature Photonics*, vol. 13, no. 8, pp. 575–579, 2019.

[19] C. Bruschini, H. Homulle, I. M. Antolovic, S. Burri, and E. Charbon, "Single-photon avalanche diode imagers in biophotonics: review and outlook," *Light: Science & Applications*, vol. 8, no. 1, p. 87, 2019.

[20] K. Hwang, T. Pan, A. Joshi, J. C. Rasmussen, W. Bangerth, and E. M. Sevick-Muraca, "Influence of excitation light rejection on forward model mismatch in optical tomography.," *Physics in medicine and biology*, vol. 51, pp. 5889–5902, nov 2006.

[21] J. Chen and X. Intes, "Time-gated perturbation Monte Carlo for whole body functional imaging in small animals.," *Optics express*, vol. 17, pp. 19566–19579, oct 2009.

[22] R. Yao, X. Intes, and Q. Fang, "Direct approach to compute Jacobians for diffuse optical tomography using perturbation Monte Carlo-based photon "replay"," *Biomedical Optics Express*, vol. 9, no. 10, pp. 4588–4603, 2018.

[23] M. A. O'Leary, *Imaging with diffuse photon density waves*. PhD thesis, University of Pennsylvania Philadelphia, 1996.

[24] A. C. Kak and M. Slaney, *Principles of Computerized Tomographic Imaging*. IEEE Press, 1988.

[25] H. K. Kim, L. D. Montejo, J. Jia, and A. H. Hielscher, "Frequency-domain optical tomographic image reconstruction algorithm with the simplified spherical harmonics (SP(3)) light propagation model.," *International journal of thermal sciences = Revue generale de thermique*, vol. 116, pp. 265–277, jun 2017.

[26] C. Liu, A. Maity, A. W. Dubrawski, A. Sabharwal, and S. G. Narasimhan, "High resolution diffuse optical tomography using short range indirect subsurface imaging," in *IEEE International Conference on Computational Photography*, IEEE, May 2020.

[27] L. Wang, S. L. Jacques, and L. Zheng, "Mcml—monte carlo modeling of light transport in multi-layered tissues," *Computer Methods and Programs in Biomedicine*, vol. 47, no. 2, pp. 131 – 146, 1995.

[28] D. Toublanc, "Henyey–greenstein and mie phase functions in monte carlo radiative transfer computations," *Appl. Opt.*, vol. 35, pp. 3270–3274, Jun 1996.

[29] A. N. Bashkatov, E. A. Genina, V. I. Kochubey, and V. V. Tuchin, "Optical properties of human cranial bone in the spectral range from 800 to 2000 nm," in *Proc.SPIE*, vol. 6163, jul 2006.

[30] A. Marjono, A. Yano, S. Okawa, F. Gao, and Y. Yamada, "Total light approach of time-domain fluorescence diffuse optical tomography.," *Optics express*, vol. 16, pp. 15268–15285, sep 2008.

[31] J. Chen and X. Intes, "Comparison of Monte Carlo methods for fluorescence molecular tomography-computational efficiency," *Medical Physics*, vol. 38, no. 10, pp. 5788–5798, 2011.

[32] A. Liebert, H. Wabnitz, N. Żołek, and R. Macdonald, "Monte Carlo algorithm for efficient simulation of time-resolved fluorescence in layered turbid media," *Optics Express*, vol. 16, no. 17, pp. 13188–13202, 2008.

[33] A. Beck and M. Teboulle, "A Fast Iterative Shrinkage-Thresholding Algorithm," *Society for Industrial and Applied Mathematics Journal on Imaging Sciences*, vol. 2, no. 1, pp. 183–202, 2009.

[34] S. Boyd, N. Parikh, E. Chu, B. Peleato, and J. Eckstein, "Distributed optimization and statistical learning via the alternating direction method of multipliers," *Found. Trends Mach. Learn.*, vol. 3, p. 1–122, Jan. 2011.

[35] A. Torricelli, A. Pifferi, L. Spinelli, R. Cubeddu, F. Martelli, S. Del Bianco, and G. Zaccanti, "Time-resolved reflectance at null source-detector separation: Improving contrast and resolution in diffuse optical imaging," *Phys. Rev. Lett.*, vol. 95, p. 078101, Aug 2005.

[36] A. Pifferi, A. Torricelli, L. Spinelli, D. Contini, R. Cubeddu, F. Martelli, G. Zaccanti, A. Tosi, A. Dalla Mora, F. Zappa, and S. Cova, "Time-resolved diffuse reflectance using small source-detector separation and fast single-photon gating," *Phys. Rev. Lett.*, vol. 100, p. 138101, Mar 2008.

[37] S. Cui, X. Zhu, W. Wang, and Y. Xie, "Calibration of a laser galvanometric scanning system by adapting a camera model," *Appl. Opt.*, vol. 48, pp. 2632–2637, May 2009.

[38] B. Comiskey, J. D. Albert, H. Yoshizawa, and J. Jacobson, "An electrophoretic ink for all-printed reflective electronic displays," *Nature*, vol. 394, no. 6690, pp. 253–255, 1998.

[39] L. A. Dempsey, M. Persad, S. Powell, D. Chitnis, and J. C. Hebden, "Geometrically complex 3D-printed phantoms for diffuse optical imaging," *Biomedical optics express*, vol. 8, pp. 1754–1762, feb 2017.

[40] J.-P. Bouchard, I. Veilleux, R. Jedidi, I. Noiseux, M. Fortin, and O. Mermut, "Reference optical phantoms for diffuse optical spectroscopy. Part 1 – Error analysis of a time resolved transmittance characterization method," *Opt. Express*, vol. 18, pp. 11495–11507, may 2010.

[41] G. D. Boreman, "Modulation Transfer Function in Optical and Electro-Optical Systems," *SPIE Press*, 2001.

[42] Micro Photon Devices, Bolzano, Italy, *FastGated SPAD Single-Photon Detection Module*, 2013.

[43] H. Li, J. Ruan, Z. Xie, H. Wang, and W. Liu, "Investigation of the critical geometric characteristics of living human skulls utilising medical image analysis techniques," *International Journal of Vehicle Safety*, vol. 2, jan 2007.

[44] M. Schweiger and S. R. Arridge, "Application of temporal filters to time resolved data in optical tomography," *Physics in Medicine and Biology*, vol. 44, pp. 1699–1717, jan 1999.